A Numerical Study of High Resolution Latent Image Formation by Laser Beam Exposure

Yoshio Watanabe, Hiroyuki Kawamoto,✦ Hisashi Shoji, Hirokatsu Suzuki, and Yumiko Kishi

Ricoh Company Ltd., Yokohama, Japan

In order to study the latent image formation process including the characteristics of laser beam and photoreceptor, a numerical method which solves the three dimensional time dependent coupled system of the transport equations for charges, and the Poisson equation for electrostatic field, is proposed. Combining the simulation with electrostatic field computation in the development zone, the strength and the extent of spreading of the electrostatic field due to the latent image is analyzed. The image of isolated one dot exposure shows larger spreading, while that of a dot alongside another dot shows weaker electrostatic-field strength. The dependence of the spreading on the beam radius indicates that the repulsion of charge due to space-charge effect becomes significant as the beam diameter decreases. The numerical results are compared with experimental ones obtained on a test bed with high resolution development, and show excellent correlation with the experimentally developed images.

Journal of Imaging Science and Technology 45: 579–585 (2001)

Introduction

In electrophotography, high resolution latent image formation is the first step in order to achieve high quality printing. As pointed out by Williams,[1] the latent image may be degraded by the lateral electrostatic field due to the neutralization of the surface charge with charge generated in the photoreceptor, and also by the mutual Coulombic repulsion of the charges in the photoreceptor. In printers and digital copiers, the small dots are formed by laser beam exposure, which generates much more dense charge in the photoreceptor than does a halogen lamp. As the dot size becomes smaller, the Coulombic repulsion becomes much more severe, because the mutual repulsive force is proportional to the square of the charge density.

Several research studies[2–4] have been carried out to investigate the latent image formation for actual dot images using the photoinduced discharge curve (PIDC) obtained from a solid image. The simulation system adopting PIDC requires only small-scale computation to predict the developed image even for the actual complex patterns. From a more physical viewpoint, the photodischarge in photoreceptors is analyzed considering mobility and quantum efficiency.[5–7] Although these investigations include the space charge effect rigorously, they are one-dimensional analyses or mainly focus on the material properties. The latent images for very small dots or thin lines generate an electrostatic field in the development zone that depends on the thickness of the photoreceptor. Extending Schaffert's[8] and Scharfe's[5] studies, the electrostatic field has been studied extensively,[9–11] and some of them demonstrate that the field strength has good correlation with the experimentally developed images of toners.

In order to study the effects of small beam spot size on the printing quality further, it is necessary to analyze the whole process, including the laser beam exposure, the charge carrier transport in the photoreceptor, and the electrostatic field in the development zone. In this article, we present a simulation system to predict the electrostatic field, especially focusing on the latent image formation with very small beam spots. When we apply the simulation to designing the laser optical system, the properties of the photoreceptor and the digital halftoning algorithm, the three-dimensional simulation is indispensable. We propose a new stable and fast numerical method that solves the charge carrier transport equations in photoreceptors. Our numerical model includes the nonlinear Coulombic mutual repulsion between charge carriers along with the generation and recombination of charges. Combining the computation of the laser beam exposure and the electrostatic field in the development zone, the electrostatic field for solid, isolated single dot and single dot alongside a neighboring dot, so-called “1 × 1”, dot exposures are simulated, and compared with the experiments of a test bed for the high resolution development.

Original manuscript received February 26, 2001

✦ IS&T Fellow

Previously presented at IS&T's NIP16: International Conference on Digital Printing Technologies, October 15-20, 2000, Vancouver, B.C. Canada.

Simulation Model of the Latent Image Formation

The simulation system consists of three steps: the first is the calculation of Gaussian laser beam exposure, the second is the simulation of the charge carrier transport process in the photoreceptor, and the third is the electro-

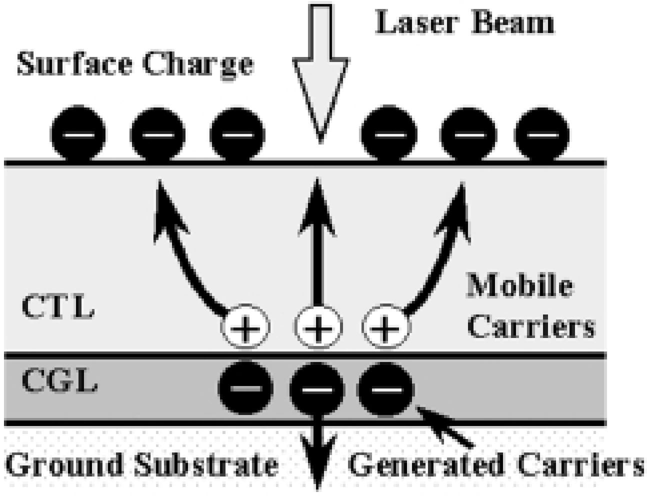

Figure 1. Schematic diagram of charge generation and transport in OPC.

static computation in the development zone. The first and the third steps can be solved using well-known methods.

The second step describes the generation and transport of charge carriers in a photoreceptor under the electrostatic field due to the surface and inner charge. Figure 1 shows the schematic diagram in a layered OPC, which will be discussed below. The mathematical representation of the process is given by

$$\frac{\partial n_p}{\partial t} + div(\mu_p \mathbf{E} n_p) = \Gamma - R n_p n_n \tag{1}$$

$$\frac{\partial n_n}{\partial t} + div(-\mu_n \mathbf{E} n_n) = \Gamma - R n_p n_n \tag{2}$$

$$div(\varepsilon \mathbf{E}) = e(n_p - n_n), \tag{3}$$

where

$$\mathbf{E} = -grad\ (\phi). \tag{4}$$

Here, n, μ, E, Γ, R, ε, e, ϕ are the number density of charge, the carrier mobility in OPC, the electric field, the charge generation rate, the charge recombination rate, the dielectric constant, the elementary electric charge, and the electric potential, respectively. The subscripts p and n indicate the quantities for the positive and negative charge, respectively.

In a layered OPC, the charge is generated in the charge generation layer (CGL) and transported in the charge transport layer (CTL). Usually the CGL can be assumed to be optically thin, which allows the charge generation rate Γ to be written as,

$$\Gamma = \beta \cdot \eta \cdot F / (d \cdot h\nu). \tag{5}$$

where β, η, F, d and $h\nu$ are the absorption and quantum efficiency of CGL, the incident laser beam flux, the thickness of CGL, and the photon energy, respectively.

The recombination terms in Eqs. 1 and 2 are introduced in order to explain the experimental results for the solid image described in the following section, which shows less generation of total charge in the CGL as the incident light becomes stronger. The absorption efficiency β represents the absorbed photons in CGL for all incident photons on the CGL. The recombination rate R and absorption efficiency β are to be determined experimentally using results from solid images.

Numerical Method

The finite difference method is used to solve the above coupled Eqs. 1, 2 and 3. We adopt the time-forward difference for the time derivatives and the upwind difference for the advection terms in Eqs. 1 and 2. All terms except the time derivatives are evaluated implicitly; namely evaluated at the $(n + 1)$th step, where n is the time step that indicates known status and the $(n + 1)$th is the future unknown step. The final form is written as:

$$\frac{n_p^{n+1} - n_p^n}{\delta t} = -\left[div(\mu_p \mathbf{E} n_p)\right]^{n+1} + \Gamma^{n+1} - R n_p^{n+1} n_n^{n+1} \tag{6}$$

$$\frac{n_n^{n+1} - n_n^n}{\delta t} = -\left[div(-\mu_n \mathbf{E} n_n)\right]^{n+1} + \Gamma^{n+1} - R n_p^{n+1} n_n^{n+1} \tag{7}$$

$$div(\varepsilon \cdot grad\phi^{n+1}) = -e(n_p^{n+1} - n_n^{n+1}), \tag{8}$$

where δt is the time interval between the successive steps. The above nonlinear algebraic Eqs. 6, 7 and 8 are solved using the "double iteration" method. The first outer iteration loop consists of successive substitution of the preceding values over the whole three equations. The inner iteration loop uses the successive over relaxation method to get the temporal solution for each equation. In the inner loop, all variables except the variable under consideration are assumed to be known by the preceding iteration steps. For example, successive over-relaxation focuses only on n_p in Eq. 6, and the other variables are treated as known.

The implicit scheme allows use of the flexible time interval δt, because it is unconditionally stable. We adopt the very small time interval when the laser beam illuminates the CGL and the very high density charge is generated, while a larger time interval is used to simulate the evolution of the charge cloud in CTL.

The numerical method is fast and requires little computer memory. The several simulations mentioned in the next sections are performed using a PENTIUM II 233MHz processor with 64MB RAM.

Test Bed System for High Resolution Development

Figure 2 shows the test bed system for high resolution development to produce isolated and 1×1 dot images at 1200 dpi experimentally. The system consists of a scorotron charger, a laser-exposure component, and a development roller around the OPC. The diameters of the development roller and the OPC are 30 mm and 100 mm, respectively. The OPC surface is charged at –870 V initially by the scorotron. The CGL of the OPC contains a triphenylamine trisazo pigment, and the CTL consists of α–phenylstilbene based charge transport material and polycarbonate.[12] The hole mobility of the CTL is about $10^{-8} \sim 10^{-9}$ m^2/Vsec under the typical electric field in electrophotography. The OPC rotates at 20.5 mm/sec for writing the OPC with the laser beam, and at 125 mm/sec for the development with the toner. We

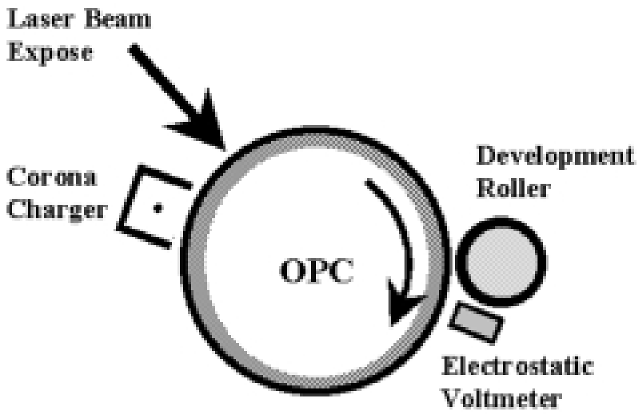

Figure 2. Test bed system for high resolution development.

adopt magnetic two-component contact development and toners with an average size of 6 μm. The gap between the OPC and the development roller is 300 μm. The experiments are carried out under the controlled condition, where the temperature is 25°C and the relative humidity is 30%. The surface voltage of the OPC is measured just after the development roller.

Numerical Results and Comparison with Test Bed Experiments

Solid Image and 1× 1 line image

Figure 3 shows the surface potential averaged over the OPC surface of solid images and 1 × 1 line images for different beam sizes and powers by the simulations and the test bed experiments. The result of 70 μm beam size of solid image with 0.21 mW is used to adjust the absorption efficiency β. If the reciprocity relation holds, the surface potential would be the same for the same laser power. However, the experimental potentials at 30 μm with 0.21 mW is greater than those for 50 μm and 70 μm beams. We assume that it is due to the recombination of charge carriers in the CGL, and fit the recombination rate R introduced in Eqs. 1 and 2 to reproduce the potential of 30 μm with 0.21 mW.

While the surface potential for the other solid image shows excellent agreement, the numerical results for 1 × 1 line are about 30~50V greater than the experimental results, which amounts to the about 10% error of the total charge generation. We suspect that it might be due to the imprecise modeling of the quantum efficiency. However, the numerical simulation reproduces well the overall dependence of the surface potential on the beam size and the power, and is therefore used to evaluate the latent image formation for various patterns.

Spatial and Temporal Features of the Simulation

As a typical example of the simulation, the numerical result for the 1200 dpi isolated single dot latent image formation will be given in Figs. 4 and 5. The upper right frame in Fig. 4 shows the schematic view of the geometry of our simulation. The horizontal direction (x-direction) corresponds to the scanning direction of the laser beam, and the vertical direction (y-direction) implies the perpendicular direction. The z-direction indicates the depth position. The laser beam shape is round with 30 μm spot size, and the power is 0.21 mW. The laser scans the OPC with 15 μm thickness by 21.7 μm

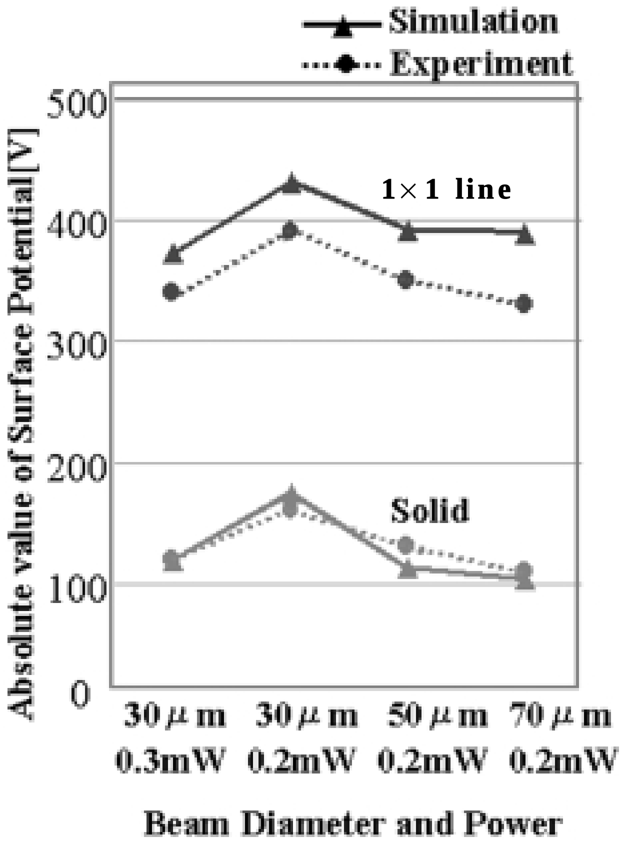

Figure 3. Simulated and experimental average surface potential for different beam sizes and powers.

in the horizontal direction (x-direction); single pixel size corresponds to 1200 dpi. Scanning makes the size of the charge cloud in the horizontal direction shown in the (x,z) plane view in Fig. 4 longer than that of the vertical one shown by the (y,z) plane view. The shades of gray in Fig. 4 show the density of the positive carriers (holes) at 50 μsec after laser irradiation.

The evolution of the charge cloud in the OPC is shown in Fig. 5. At first, very high density carriers are generated in the CGL, and move upward slowly with gradual decrease of the central density. If there were no space charge density effect, the transit time of the carrier would be about 140 μsec under these conditions. However, the simulation shows that the center still remains less than 5 μm high, which is one-third of the OPC thickness. The leading edge of the carrier cloud seems to be spaced out on the OPC surface, and the center of the cloud arrives at the surface after 400 μsec, or later. In the figure, the profile of the carrier cloud appears to be shrinking with time, but this is due to the shading method that uses the absolute value of carrier density. While the density itself decreases with time, the overall profile becomes correspondingly wider, which results in the spreading of the final surface charge profile.

Isolated 1 Dot Image

In order to clarify the correlation between the simulation and the actual development, the simulated electric fields for isolated single dot and 1 × 1 dot images are compared with the experimentally developed images using the high resolution test bed mentioned in the preceding section. Figure 6 shows the case for the

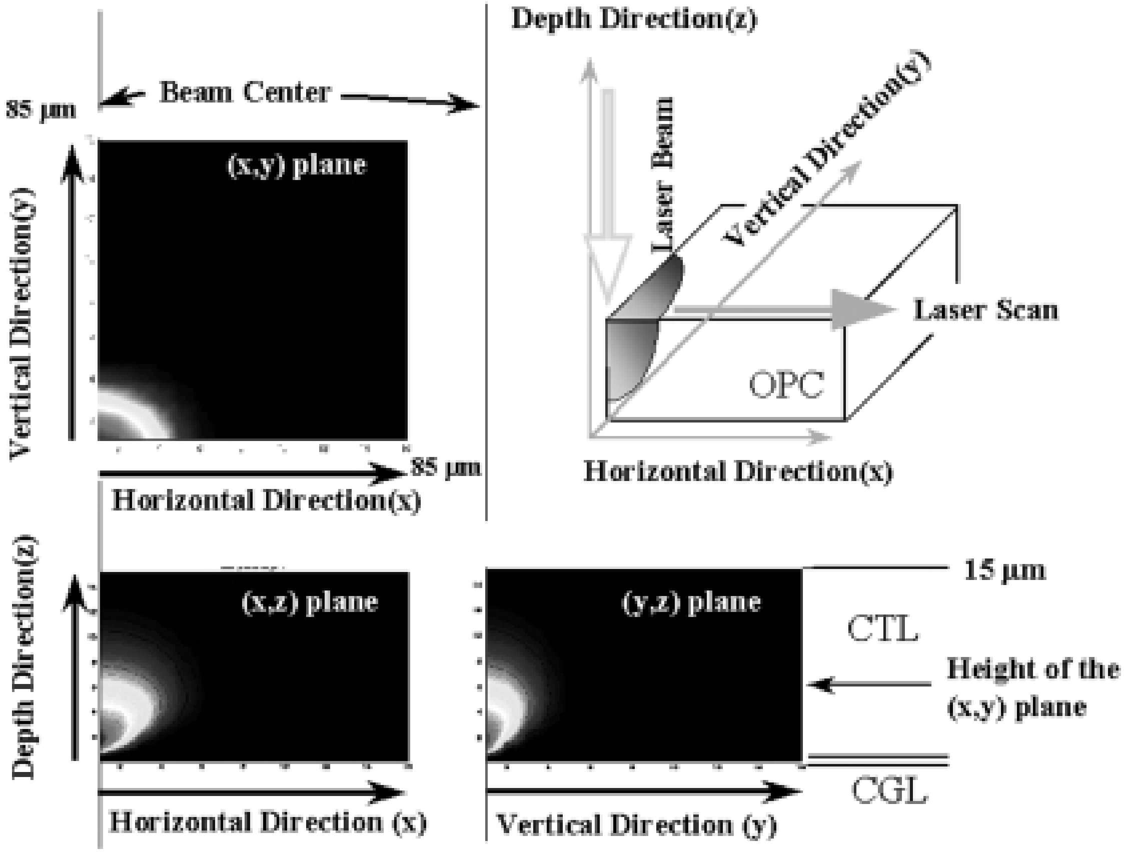

Figure 4. Three-dimensional view of charge (hole) density at 50 µsec. The laser beam spot size is 30 µm and the OPC thickness is 15 µm. The upper right frame shows the coordinate system and the laser scanning.

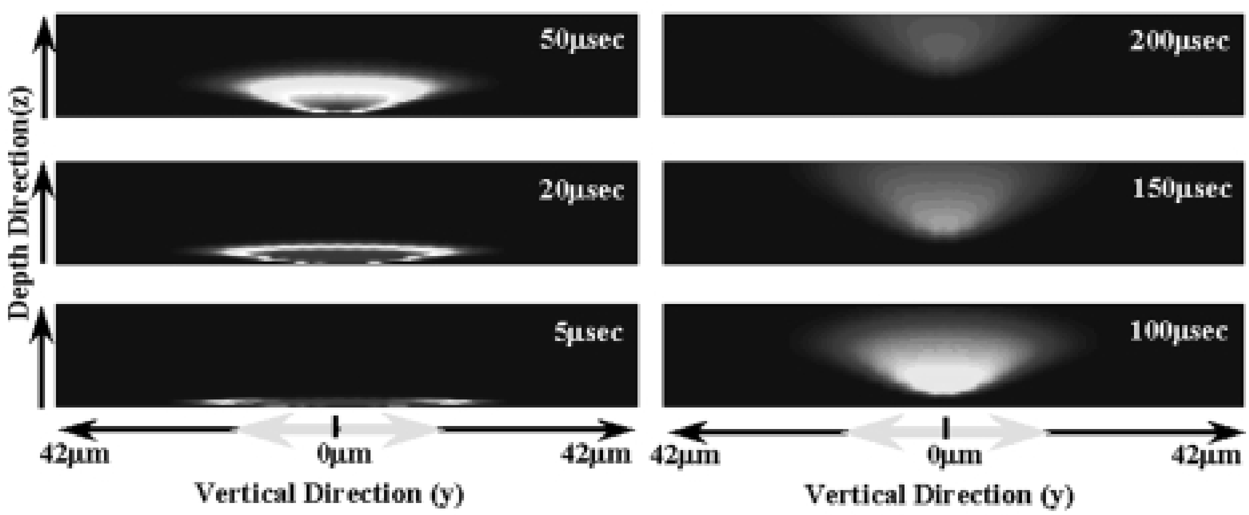

Figure 5. The evolution of positive charge carrier (hole) cloud. The figures show the cross-sections normal to horizontal direction (the scanning direction). The $1/e^2$ beam spot size is 30 µm which is indicated by the horizontal arrows, and the thickness of the OPC is 15 µm.

isolated single dot images formed by the laser beam with 0.21 mW power. The inner four frames are the electric field and laser beam exposure profiles normalized for the maximum and minimum of the field strength. The outer four frames are the experimental images. The simulation is carried out for 30 µm and 50 µm beam sizes and for 15 µm and 28 µm thick OPC as indicated in the figure.

The upper left results for 28 µm thick OPC with 30 µm beam shows the largest spreading of the profile, which can be seen from the much broader profile of the electric field compared to the incident laser pro-

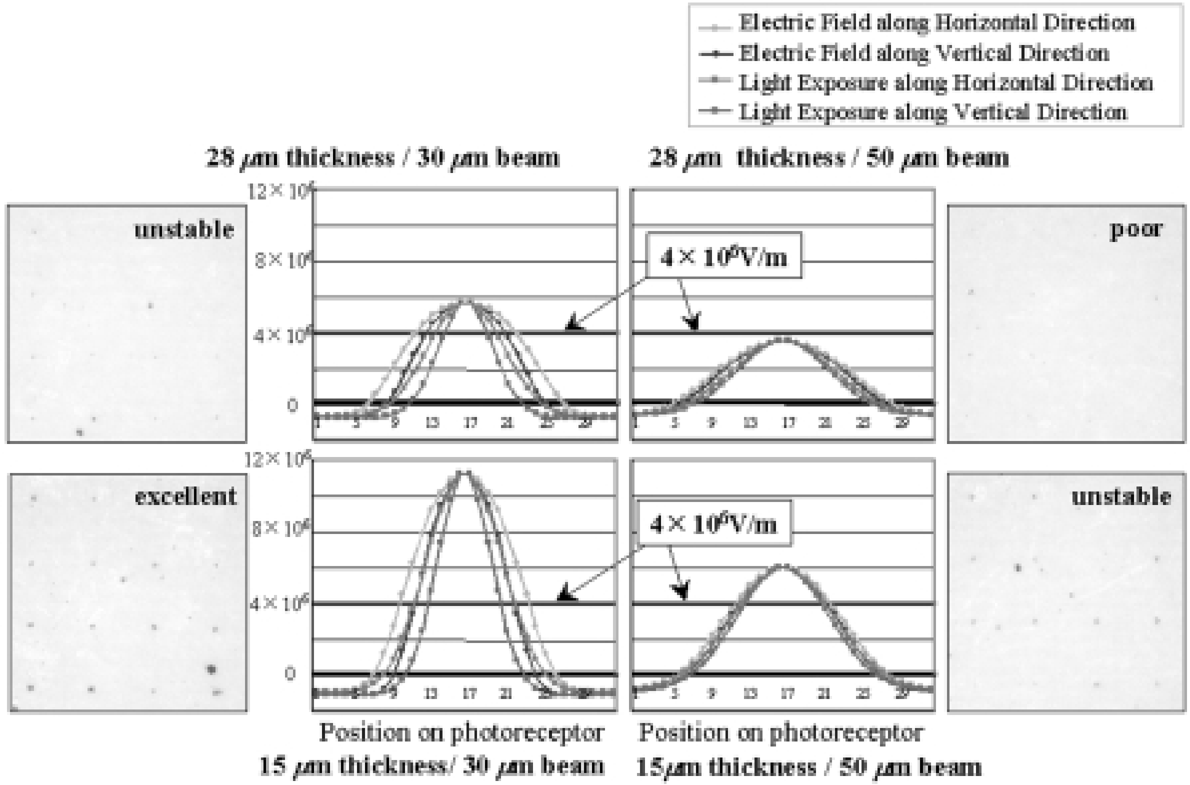

Figure 6. Electric field strength and light exposure for isolated single dot with experimentally developed images.

file. Slight spreading is recognized even for the 50 μm beam.

The lower results are for 15 μm thick OPC. The 30 μm beam result shows much higher field strength, and the experiment also shows excellent quality image, but the spreading is rather large. The spreading is due to the mutual repulsion of charge carriers. The lower right frame shows results for the 50 μm beam, which shows little spreading even though the total number of generated charge carriers and the initial field strength is the same as for the left-hand, 30 μm, case. It indicates that the mutual repulsion becomes much more severe with smaller beam spot size.

The strength of the numerical electric field shows good correlation with the quality of the experimental development images; the threshold giving excellent image quality is about 4×10^6 V/m, which is marked in the figure. Our threshold is approximately the same as the threshold 3.21×10^6 V/m given by Allen and Coit[11] for high power exposure corresponding to our case, though the development systems are different in each case.

1 × 1 Dot Image

Figure 7 shows the numerical and experimental results for 1 × 1 dot images under the same conditions at the isolated single dot results. The spreading of the latent image is less than that for the isolated single dot, because the neighboring dots suppress expansion of the charge cloud. The 30 μm beam gives large spreading even for the thinner OPC, but the amount is smaller than that for isolated dot. On the other hand, the strength of the electric field is lower than that for the isolated dot, because the edge effect is decreased by the neighboring dots. The threshold for good quality image is 2.5×10^6 V/m, which is lower than that for the isolated dot, but might reflect characteristics of the test bed development system.

Summary of the Numerical Results

Figure 8 summarizes the electric field strength for various beam spot sizes and OPC thicknesses mentioned above as well as the results for a 10 μm thick OPC. As expected, the field strength of the isolated dot is greater than that for the 1 × 1 dot case, which indicates that the neighboring charges in the 1 × 1 dot image suppress the field strength. Also the field strength for the 30 μm beam is twice as large as that for 50 μm in the isolated dot case, while in the case of the 1 × 1 dot this discrepancy becomes more significant. We attribute this result to the spiked or rippled surface charge profile formed by the 30 μm beam which makes a much stronger electric field owing to the edge effect, than the "smeared-out" charge profile of the 50 μm beam.

Finally, the spreading ratios of the electric field in the vertical direction to the incident laser beam profile are shown in Fig. 9. The ratio for the isolated dot image is greater than that for the 1 × 1 dot image. The spreading ratio for the 30 μm beam is much greater than that for the 50 μm beam profile. In the 30 μm beam case, spreading remains even with the 10 μm thick OPC, which demonstrates that the Coulombic mutual repulsion of charge carriers still occurs even for such a thin OPC.

Conclusion

In order to simulate three dimensional latent image formation, we propose a new numerical "double iteration" method for the implicit finite difference equation for the charge transport equations and the Poisson equation for electrostatic field. The method is fast and stable, and requires less computer resources. The computed elec-

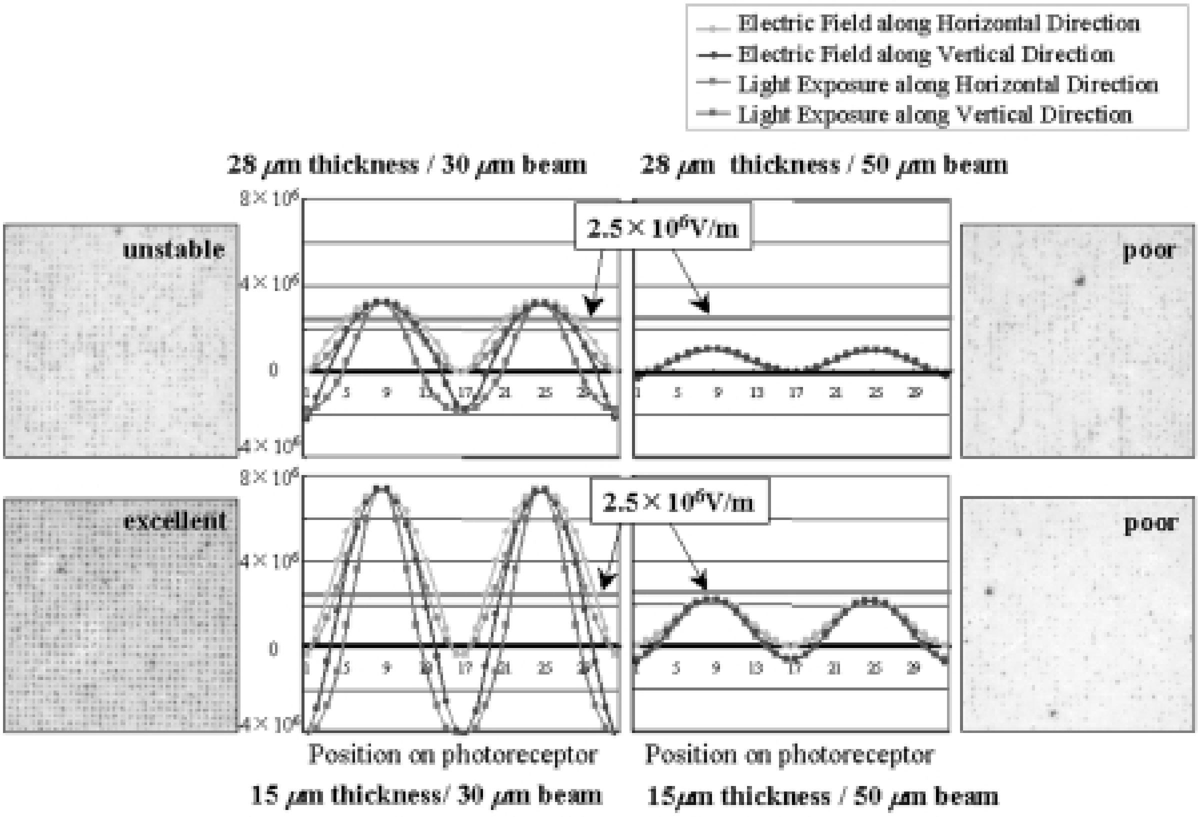

Figure 7. Electric field strength and light exposure for 1 × 1 dot with experimentally developed images.

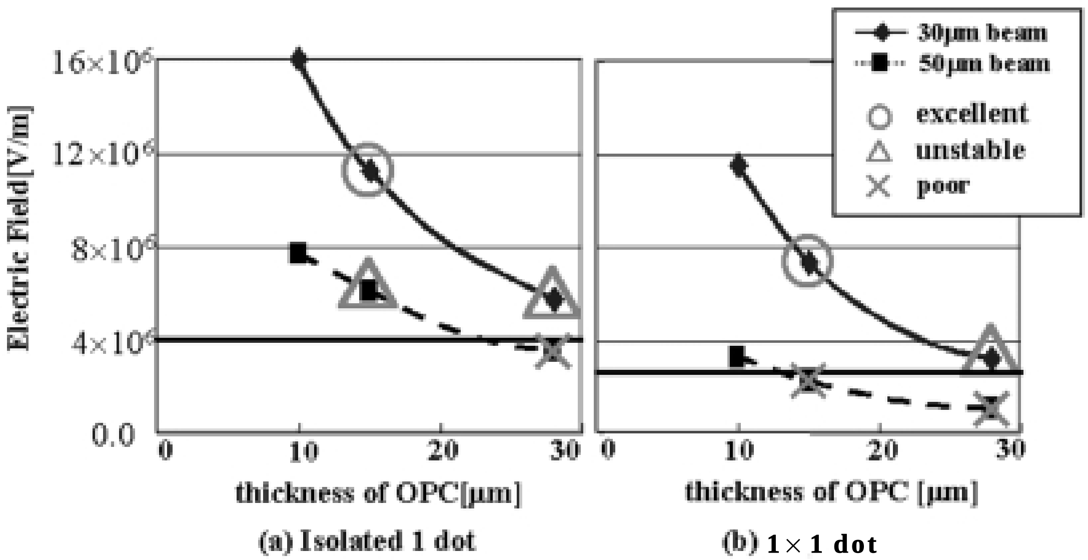

Figure 8. Maximum electric field for various beam spot size and OPC thickness. The bold horizontal lines indicate the threshold for good image quality. The circular, triangular and cross marks express the excellent, unstable and poor experimentally developed images, respectively.

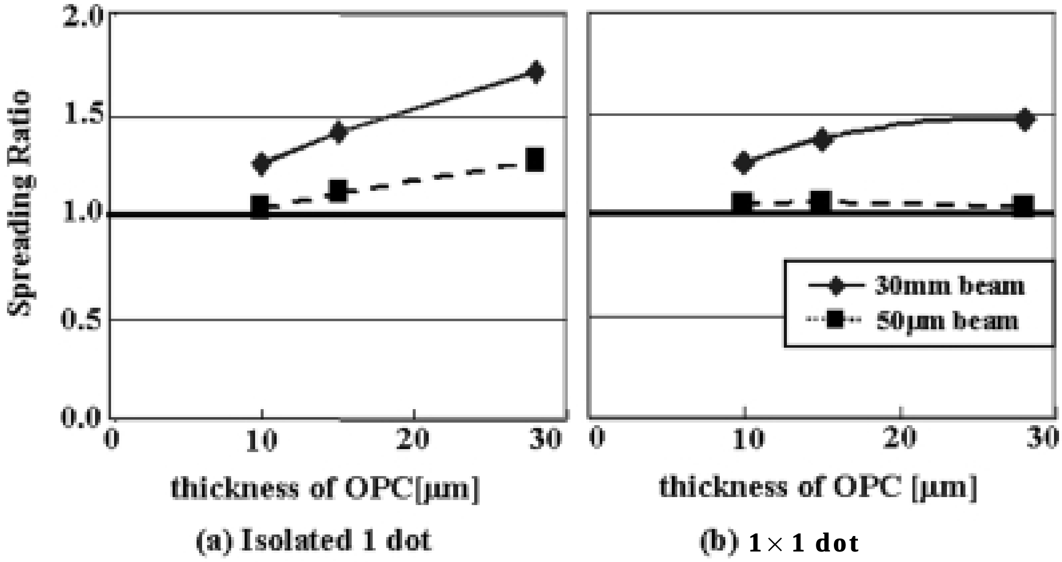

Figure 9. Spreading ratio of the electric field to the incident laser profile for various beam spot sizes and OPC thicknesses.

tric field strength shows good correlation with the experimental results from a test bed development system, though the threshold depends on the image pattern. It shows that the latent image of an isolated dot produced by a 30 μm laser beam exhibits a large spreading of charge carriers, brought about by the mutual repulsion between charge carriers. The proposed simulation method allows us to design the beam radius, power and the OPC properties considering the effects of the latent image pattern.

Acknowledgment. The authors are grateful to their colleague Mr. Masami Kadonaga for his discussions and to Dr. Lawrence B. Schein, consultant, for his valuable suggestions on the development process. The authors also wish to thank Mr. Koji Hirakura, the general manager of RICOH Research and Development Center, for his encouragement to publish our investigation.

References

1. E. M. Williams, *The Physics and Technology of Xerographic Processes*, John Wiley and Sons, New York, 1984, p.30.
2. N. Kawamura and M. Itoh, *Electrophotography*, **26**, 364 (1987).
3. T. Motoi, *Konica Technical Report*, **5**, 89 (1992).
4. T. Kagawa, T. Makiura, N. Nakano and T. Toyoshima, *Sharp Technical Report*, **76**, 46 (2000).
5. M. Scharfe, *Electrophotography Principles and Optimization*, Research Studies Press, 1984, Chap.4.
6. P. M. Borsenberger and D. S. Weiss, *Organic Photoreceptors for Xerography*, Marcel Dekker, New York, 1998, p. 39.
7. K. Oka and S. Fujiwara, *J. Imaging Soc. Japan*, **38**, 296 (1999).
8. R. M. Shaffert, *Electrophotography*, 2nd ed., Focal Press, London, 1975.
9. H. Imada, A. Hakamoto, T. Higashiguchi, H. Kiwaki, and S. Takeuchi, *Electrophotography*, **32**, 253 (1993).
10. T. Iwamatsu, T. Toyoshima, N. Azuma, M. Yoshinori, and Y. Nakajima, in *Proc. IS&T's NIP 15: 1999 Int'l. Conference on Digital Printing Technologies*, IS&T, Springfield, VA 1999, pp.732–735.
11. J. B. Allen and A. B. S. Coit, *J. Imaging Sci. Technol.* **43**, 309 (1999).
12. Y. Sakon, T. Suzuki and M. Umeda, *J. Imaging Soc. Japan*, **38**, 20 (1999).